Supporting Information

Accelerating Industrial-level CO$_2$ Electroreduction Kinetics on Isolated Zinc Centers via Sulfur-boosting Bicarbonate Dissociation

Wanzhen Zheng,[†a] Dashuai Wang,[†b] Wenjun Cui,[d] Xiahan Sang,[d] Xuetao Qin,[h] Zilin Zhao,[a] Zhongjian Li,[a] Bin Yang,[a] Miao Zhong,[e] Lecheng Lei,[a,b] Qiang Zheng,[f] Siyu Yao,[a] Gang Wu,[*g] Yang Hou[*a,b,c]

[a] Key Laboratory of Biomass Chemical Engineering of Ministry of Education, College of Chemical and Biological Engineering, Zhejiang University, Hangzhou 310027, China

[b] Institute of Zhejiang University - Quzhou, Quzhou 324000, China

[c] Donghai Laboratory, Zhoushan, China

[d] Research and Testing Centre of Material School of Materials Science and Engineering, Wuhan University of Technology, Wuhan 430070, China

[e] College of Engineering and Applied Sciences, National Laboratory of Solid State Microstructures, Collaborative Innovation Center of Advanced Microstructure, Jiangsu Key Laboratory of Artificial Functional Materials, Nanjing University, Nanjing 210023, China

[f] CAS Key Laboratory of Standardization and Measurement for Nanotechnology, CAS Center for Excellence in Nanoscience, National Center for Nanoscience and Technology, Beijing, 100190, China

[g] Department of Chemical and Biological Engineering, University at Buffalo, the State University of New York Buffalo, NY, 14260, United States

[h] Beijing National Laboratory for Molecular Sciences, College of Chemistry and Molecular Engineering and College of Engineering, and BIC-ESAT, Peking University, Beijing 100871, China

[†] These authors contributed equally.

Section S.1 Material synthesis

S.1.1 Synthesis of ZIF-8 and ZIF-8-S precursors

2-methylimidazole (13.14 g) was dissolved in methanol (400 mL) under stirring, followed by dropwise adding 400 mL of methanol solution containing 5.80 g of $Zn(NO_3)_2$ $6H_2O$. The above mixed solution was further stirred for 1 h, collected by centrifugation, and dried in oven at 60 °C for 12 h under vacuum.

ZIF-8-S precursor was prepared via a solvent-assisted linker exchange process by adding 300 mg of 5-Amino-1,2,3-thiadiazole into 60 mL of ZIF-8 (150 mg) in suspended methanol solution, and stirred for another 48 h. The final nanocrystals were collected by centrifugation and washed by methanol for more than 3 times to remove redundant organic linkers, and dried in oven at 60 °C for 12 h under vacuum.

S.1.2 Synthesis of Zn-N-C and Zn-NS-C

The Zn-N-C and Zn-NS-C were synthesized by carbonizing the ZIF-8 and ZIF-8-S precursors under Ar atmosphere at 1100 °C for 2 h, respectively.

S.1.3 Synthesis of Zn-NS$_X$-C (X = S doping content)

The Zn-NS$_x$-C samples with different S doping contents were synthesized following the same procedure as the Zn-NS-C, but by adjusting the mass ratios of ZIF-8 and 5-Amino-1,2,3-thiadiazole, or adjusting the time for linker exchange.

S.1.4 Synthesis of Zn-NS-C-Y (Y = carbonization temperature of 800, 900, 1000, 1100 °C)

The Zn-NS-C-Y samples obtained at different carbonization temperatures were synthesized following the same procedure as the Zn-NS-C, but by changing the final carbonization temperatures of ZIF-8-S.

S.1.5 Synthesis of Zn-NS-C-Z (Z = Size of ZIF-8)

The Zn-NS-C-Z samples with different particle sizes were synthesized following the same procedure as the Zn-NS-C, but by controlling the concentrations of $Zn(NO_3)_2$ $6H_2O$ and 2-methylimidazole in methanol when synthesized the ZIF-8.

Section S.2 Characterizations

FESEM (SU-8010, Hitachi), TEM (HT-7700, Hitachi) and HRTEM-STEM (Titan Cubed Themis G2 300) are used to determine the morphology of as-prepared catalysts. X-ray diffractometer (PANalytical X'Pert PRO) is used to analyze the phase composition of as-prepared catalysts. The analysis of elemental composition and its chemical environment is performed determined by X-ray photoelectron spectrometer (Thermo Fisher Scientific, Escalab 250 Xi XPS with an Al Kα X-ray resource). The pore size and BET surface area of as-prepared catalysts are measured on Micromeritics® TriStar II Plus. The content of Zn species in as-prepared catalysts is quantified by ICP-OES (Agilent 700-ES/Vista Axial). Raman spectra of as-prepared catalysts are performed on HORIBA/XploRA PLUS. The XAS experiments of as-prepared catalysts are performed at the 1W1B station in Beijing Synchrotron Radiation Facility and Shanghai Synchrotron Radiation Facility BL14W1. Liquid-phase products after CO_2ER are quantified by ^1HNMR spectroscopy (BRUKER AVANCE III 600). The *in-situ* FTIR-ATR spectra of as-prepared catalysts are detected on BRUKER INVENIO R. The device for testing *in-situ* FTIR-ATR spectra is purchased from Shanghai Yuanfang Technology Co., LTD.

Section S.3 Preparation of working electrode

S.3.1 Preparation of working electrode in H-cell.

5 mg of catalyst was dispersed in 450 μL of ethanol and 50 μL of 0.5 wt.% Nafion solution (D520, DuPont) under ultrasonic for 1 h to prepare a homogeneous ink. Then, 60 μL of homogeneous ink was dropped onto the carbon paper (3 × 1 cm², HP030, Hesen) and dried in a vacuum, with the catalyst mass loading of 0.6 mg cm⁻². The geometric reaction area of the cathode was controlled to be 1 × 1 cm² (Fig. S23b).

S.3.2 Preparation of working electrode in flow cell.

24 mg of catalyst (Zn-NS-C) was dispersed in 5 mL of methanol and 250 μL of 5 wt.% Nafion solution (D520, DuPont) under ultrasonic for several hours to prepare a homogeneous ink. Then, the well-proportioned homogeneous ink was fully air-brushed onto the gas diffusion electrode (Sigracet 29 BC, 4 × 2 cm²) and dried in a vacuum,

with the catalyst mass loading of 3.0 mg cm^{-2}. The geometric reaction area of the cathode was 1.0×0.5 cm².

S.3.3 Preparation of tandem Zn-NS-C/Cu/PTFE electrode in flow cell.

The Cu target was firstly deposited onto the surface of polytetrafluoroethylene (PTFE, with an average pore size of 100 nm) substrate by a magnetron sputtering method. Further, the Zn-NS-C catalyst ink was spray-deposited onto the Cu/PTFE substrate with a final loading amount of 0.5 mg cm^{-2}, and the geometric reaction area of cathode was 1.0×0.5 cm².

Section S.4 Electrochemical measurements in H-cell.

The H-cell consisted of two gas-tight glass compartments and a cation exchange membrane (Nafion 117, DuPont) was sandwiched between the two compartments to separate the anodic and cathodic electrolytes (Fig. S23a). The anodic and cathodic electrolytes were stagnant 0.5 M KHCO$_3$ solutions. Before the performance tests of the as-prepared catalysts, the highly purified CO$_2$ gas (99.999%) was injected continuously into the cathodic electrolyte with a flow rate of 60 mL min^{-1} for at least 30 min to obtain a CO$_2$-saturated electrolyte. During the testing process, the cathodic electrolyte was constantly stirred under 600 rpm using a magnetic stirring; while the highly purified CO$_2$ (99.999%) was injected continuously into the cathodic electrolyte with a flow rate of 20 mL min^{-1}. The continuously flowing CO$_2$ not only keep the electrolyte saturated with CO$_2$, but also carry the gaseous products directly into the gas chromatography (GC). The electrochemical tests of as-prepared catalysts in H-cell were performed on CHI760E with a three-electrode system, in which the anode is the Pt mesh electrode, the cathode is the as-prepared catalyst loaded on carbon paper, and the reference electrode is Ag/AgCl electrode.

Section S.5 Measurements of CO$_2$ diffusion boundary layer thickness in H-cell.

The electroreduction reaction of ferricyanide was used to probe the layer thickness of hydrodynamic boundary in our H-cell, since the reduction rate of ferricyanide is limited only by the mass transfer regardless of the applied potentials.[1] Notably, the test conditions of ferricyanide electroreduction were the same as that we used to test the CO$_2$ER performances of as-prepared catalysts, except the extra added 10 mM of

$K_3Fe(CN)_6$ into the cathodic electrolyte, and changed the working electrode to a commercial Au electrode (Fig. S23b), which can avoid the Galvanic corrosion process. As shown in Fig. S23c, the diffusion-limited current density plateau for ferricyanide reduction (from 0.6 to -0.4 V vs. RHE) can be identified in the cyclic voltammetry (CV) curves. Taking the middle point within plateau range as the applied potential (0.1 V vs. RHE) to perform the chronoamperometry curve (Fig. S23d), a steady-state ferricyanide diffusion-limited current density can be measured and the related hydrodynamic boundary layer thickness for ferricyanide transfer is calculated by the Fick's law:

$$\delta_{BL} = \frac{F \times D_{Fe(CN)_6^{3-}} \times C_{Fe(CN)_6^{3-}}}{j_{ss}}$$

where δ_{BL} is the hydrodynamic boundary layer thickness for ferricyanide transfer; F is the Faraday constant, 96485 C mol^{-1}; $D_{Fe(CN)_6^{3-}}$ is the diffusion coefficient of ferricyanide ion, 0.72×10^{-5} cm^2 s^{-1}; $C_{Fe(CN)_6^{3-}}$ is the concentration of ferricyanide ion in bulk electrolyte, 10 mM; j_{ss} is the measured steady-state ferricyanide diffusion-limited current density. In our H-cell, under the same test conditions as CO$_2$ER, the corresponding j_{ss} was measured to be 3.6 mA cm^{-2}, as the δ_{BL} for ferricyanide transfer was calculated to be 19.3 µm.

The boundary layer thickness for dissolved CO$_2$ transfer (δ_{CO2}) can be calculated by the equation[2]:

$$\delta_{CO_2} = \delta_{BL} (\frac{D_{CO_2}}{D_{Fe(CN)_6^{3-}}})^{1/3}$$

where D_{CO2} is the diffusion coefficient of CO$_2$, 1.92×10^{-5} cm^2 s^{-1}. Therefore, under the testing conditions we used, the δ_{CO2} in our H-cell was determined to be 26.8 µm.

The CO$_2$ mass transfer-limited current density for CO$_2$ER can be calculated by the following equation:

$$j_{limit} = \frac{n \times F \times D_{CO_2} \times C_{CO_2}}{\delta_{CO_2}}$$

where n is the number of transferred electrons related to yield CO$_2$ER products ($n = 2$ for CO formation), F is the Faraday constant, 96485 C mol^{-1}, C_{CO2} is the saturated

concentration of CO_2 in bulk electrolyte (C_{CO2} = 34 mM at 25 °C and 1.0 atm, according to the Henry's law). Based on the calculated δ_{CO2} of 26.8 μm, the j_{limit} for electrochemical CO_2-to-CO conversion ($j_{limit,CO}$) in our H-cell was determined to be 47 mA cm^{-2}.

Section S.6 Electrochemical measurements in flow cell

The detailed construction of the flow cell was shown in Fig. S31 and Fig. S32. The electrochemical performance test of as-prepared catalysts in flow cell was performed on CHI760E with a three-electrode system, in which the anode is Ni foam, the cathode is as-prepared catalyst loaded on gas diffusion layer (GDL), and the reference electrode is Ag/AgCl electrode. During the testing process, a cation exchange membrane (Nafion 117, DuPont) was sandwiched between the anolyte and catholyte flow field, and 1.0 M $KHCO_3$ solution was circulated in anolyte and catholyte flow field separately with a flow rate of 10 mL min^{-1}; the highly purified CO_2 (99.999%) was injected continuously along the backside of the GDL with a flow rate of 20 mL min^{-1}.

Unless otherwise specified, all the related potentials were cathodic half-reaction potential, and were calculated to versus reversible hydrogen electrode (RHE) following the equation:

$$E_{RHE} = E_{Ag/AgCl} + 0.197 + 0.0591 \times pH + i \times R_S$$

where i is the applied cathodic current (A), $E_{Ag/AgCl}$ is the recorded cathodic half-reaction potential, the solution resistance (R_S) was determined by electrochemical impedance spectrum (EIS) at AC voltage of 10 mV amplitude with frequency range between 10^5 and 10^{-3} Hz. All the potentials versus reversible hydrogen electrode were manually compensated.

Linear sweep voltammetry (LSV) curve was performed at a potential range from 0 to -1.2 V with a scan rate of 5 mV s^{-1}. The concentration of gaseous products was quantified by GC to calculate the faradaic efficiency (FE) of corresponding gas products following the equation:

$$FE = \frac{j_i}{j_{total}} \times 100\% = \frac{X_i \times v \times \frac{n_i FP}{RT}}{j_{total}} \times 100\%$$

where X_i is volume fraction of product quantified by GC (mL mL^{-1}), v is flow rate of gas (mL s^{-1}), n_i is number of transferred electrons.

The liquid products were analyzed by ^{1}H nuclear magnetic resonance (^{1}H NMR) spectrum, in which 400 μL of the electrolyte after CO$_2$ER test was mixed with 100 μL of 10 mM dimethyl sulfoxide solution (DMSO/D$_2$O). The DMSO was used as the internal standard, while a solvent suppression method was adopted to decrease the intensity of H$_2$O peak to make the peaks of liquid-phase CO$_2$ER products more visible.

Section S.7 Measurement of bicarbonate order dependence

The measurements were done by varying the concentrations of potassium bicarbonate from 0.1 M to 0.5 M in the electrolyte, while keeping the K$^+$ concentration to 0.5 M by adding potassium chloride. Thus, the potential influence of K$^+$ cations on increasing the strength of the electric field in the cathode Helmholtz double layer could be negligible. Besides, the potentials in the SHE scale were applied to test the CO$_2$ER performance because the potential is in nature regardless of pH; meanwhile, the potential located at the linear region of the Tafel slope was applied to exclude the influence of non-kinetic factors during the CO$_2$ER; and then, the J_{CO} measured at -0.85 V vs. SHE was set as the characteristic index.

Section S.8 Measurement of kinetic isotope effect

For KIE experiments, the CO$_2$ER measurements of Zn-NS-C and Zn-NS$_{2.8}$-C were performed both in 0.5 M KHCO$_3$/D$_2$O solution and 0.5 M KHCO$_3$/H$_2$O solution. The mass loading of as-prepared catalysts on cathode was fixed to be 0.6 mg cm^{-2}, and the KIE values were calculated by R_{CO} in H$_2$O divide R_{CO} in D$_2$O measured at -0.92 V vs. SHE.

Section S.9 Computational methods

The first principles calculations were employed by the Vienna ab initio simulation package.[3] A plane wave cutoff energy of 400 eV was used. The generalized gradient approximation proposed by Perdew, Burke, and Ernzerhof was used in the projector-augmented wave method.[4, 5] The Grimme's D3 scheme method for van der Waals (vdW) interactions was used to characterize the weak interaction.[6] ZnN$_4$ structure were constructed in 6 × 3√3 supercell. Because of periodic boundary conditions, a vacuum

layer of 15 Å between two neighboring layer units was used. For the optimization and self-consistent calculations, the Brillouin zone was sampled using the Monkhorst−Pack scheme.[7] Ionic and electronic relaxations were performed by applying a convergence criterion of 0.05 eV/Å per ion and 10^{-5} eV per electronic step, respectively. $G(CO_2)$ and $G(CO)$ were calculated from $C(s) + O_2(g) = CO_2(g)$ and $2C(s) + O_2(g) = 2CO(g)$, and Gibbs free energies of each reaction intermediate were given by the following equation: $G = E_{DFT} + E_{ZPE} - TS$, where E_{DFT}, E_{ZPE}, T, and S are total energy by DFT calculations, the zero-point energy, temperature (300 K), and entropy, respectively.[8] The entropies of adsorbed molecules (TS) were calculated from the vibrational frequencies associated with the normal modes in the harmonic approximation. The Poisson-Boltzmann (PB) implicit solvation model, Vaspsol[9], was used to describe the effect of solvation as implemented in VASP. The electrode potential, U (vs. reversible hydrogen electrode), is considered by $\Delta Gn (U) = \Delta Gn (U = 0) + neU$ when n electrons are transferred. The pH effect is introduced by correcting the $G(H^+)$ with $-kT\ln(1/[H^+])$. The climbing-image nudged elastic band method was conducted determine reaction barriers.[10]

Fig. S1 Illustration for the synthetic process of Zn-NS-C and Zn-N-C.

The ZIF-8 with well-defined Zn-N$_4$ nodes (the Zn^{2+} nodes tetrahedral coordinated by four N atoms from 2-methylimidazole linkers) was used as the precursor,[11] then the 2-methylimidazole linkers in the ZIF-8 was partially replaced by the 5-amino-1,2,3-thiadiazole linker that internally possess the 'N-S' bonds in the framework.[12-14] With such an optimal pre-modify strategy, the precursor of ZIF-8 with proper S doping (ZIF-8-S) was obtained; the Zn-NS-C was finally synthesized by carbonizing the ZIF-8-S precursor. After carbonization, the linkers in the ZIF-8 and ZIF-8-S precursors preferred to form the graphited carbon. The tetrahedral Zn-N$_4$ nodes was transformed to the individual distributed Zn-N$_4$ sites anchored on the carbon frameworks,[11] while the "N-S" bonds in 5-amino-1,2,3-thiadiazole might provide the traction to anchor the S atoms doped surrounding the Zn-N$_4$ sites.
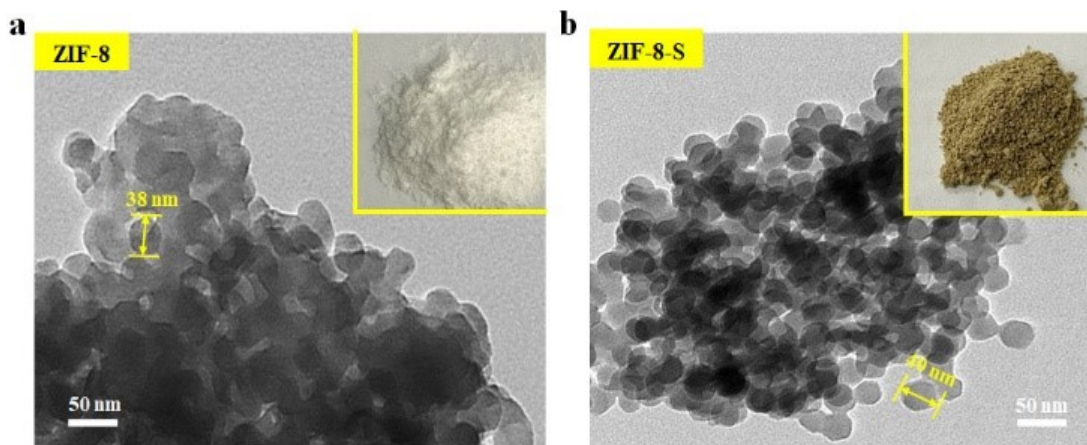
Fig. S2 TEM images of a) ZIF-8 and b) ZIF-8-S, inset: the digital photographs showing colors of ZIF-8 and ZIF-8-S.
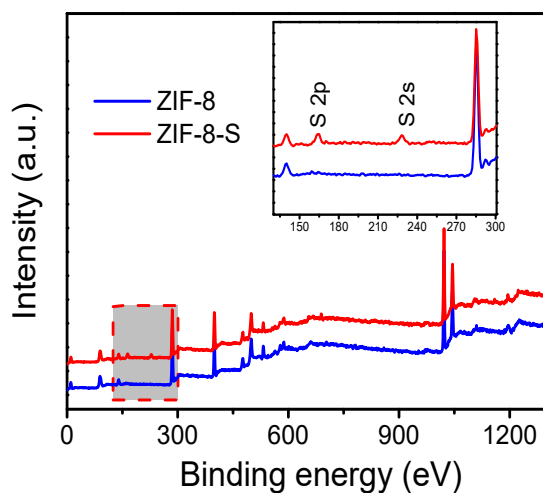
Fig. S3 The XPS survey spectra of ZIF-8 and ZIF-8-S.

The TEM images of ZIF-8 and ZIF-8-S (Fig. S2) showed the unchanged dodecahedral morphology with particle size of ~40 nm, but a distinct change in color was observed after solvent assisted linker exchange reaction. The XPS survey spectrum of ZIF-8-S displayed the characteristic peaks related to the S species (Fig. S3). These results demonstrated the successful replacement of 2-methylimidazole by 5-amino-1,2,3-thiadiazole in the ZIF-8-S.
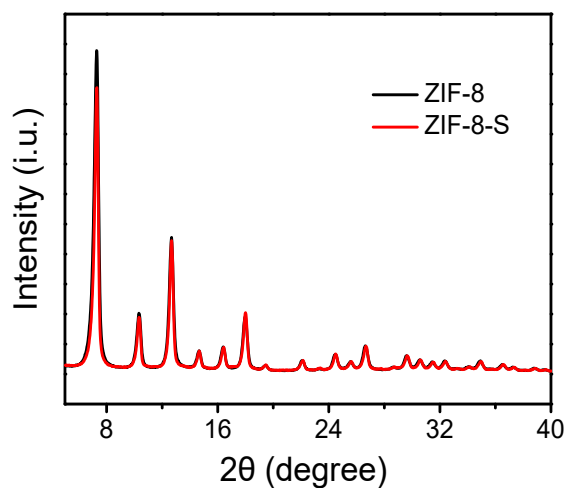
Fig. S4 The XRD patterns of ZIF-8 and ZIF-8-S.
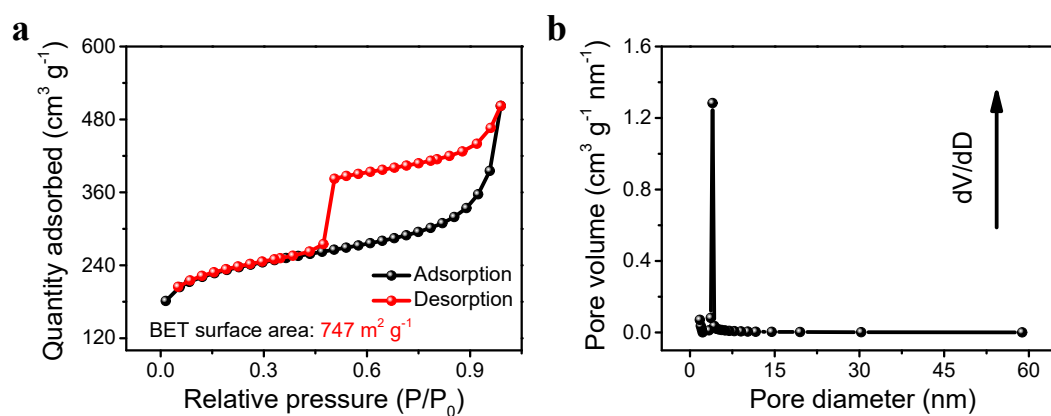
Fig. S5 The (a) N_2 adsorption and desorption curve, and (b) pore size distribution plot of Zn-NS-C.
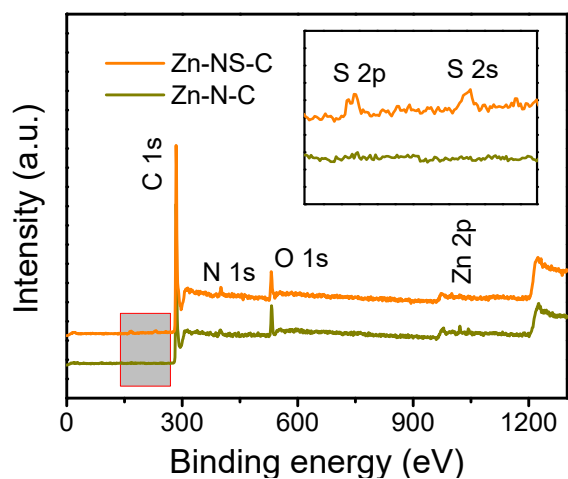
Fig. S6 The XPS survey spectra of Zn-NS-C and Zn-N-C.
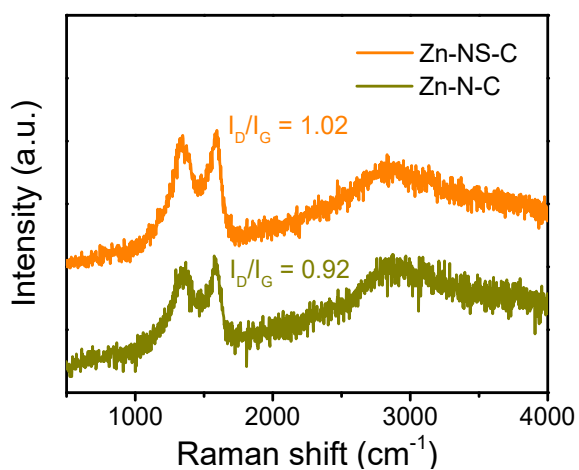
Fig. S7 The Raman spectra of Zn-NS-C and Zn-N-C.
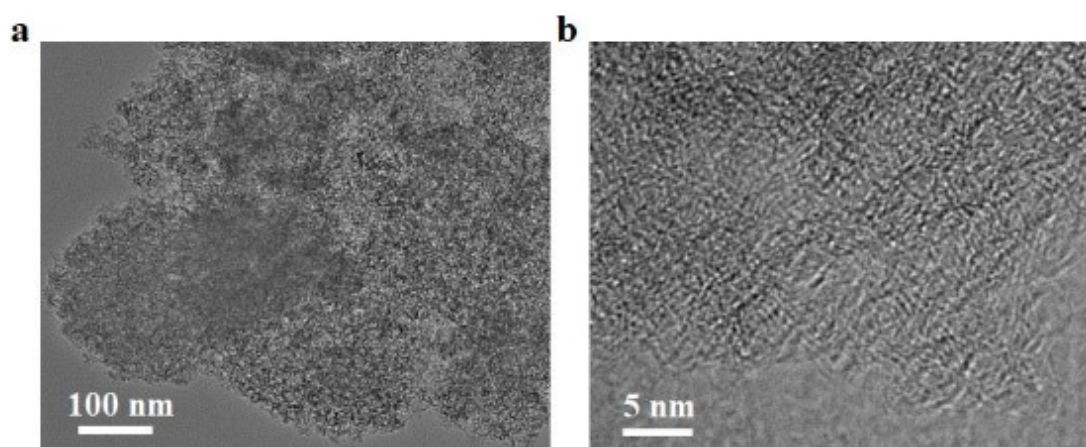
Fig. S8 (a) TEM and (b) HRTEM images of Zn-NS-C.
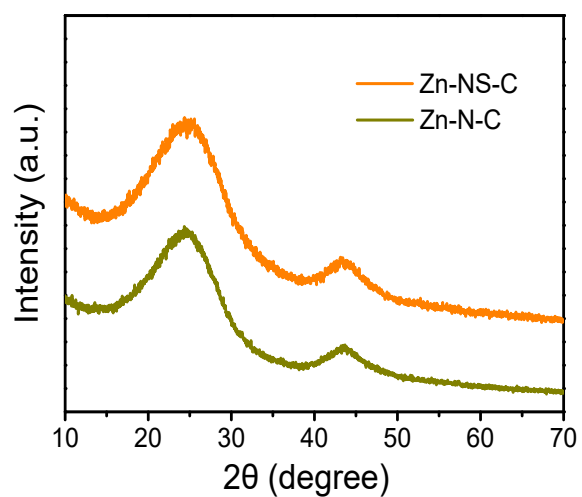
Fig. S9 The XRD patterns of Zn-NS-C and Zn-N-C.
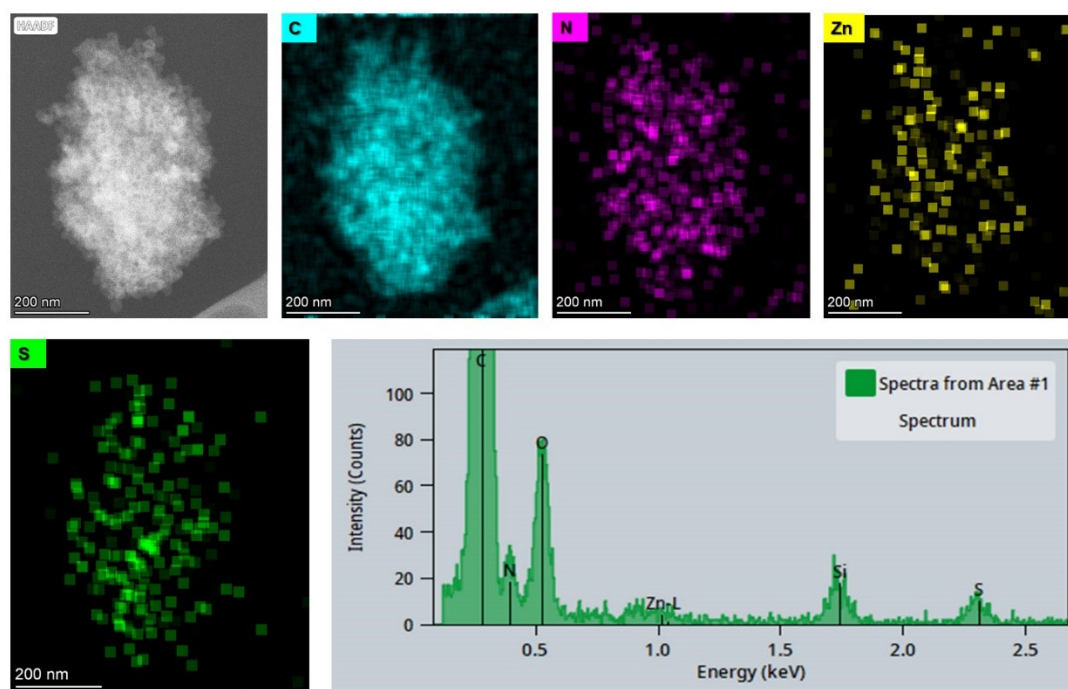
Fig. S10 The EDX elemental mapping images of Zn-NS-C.
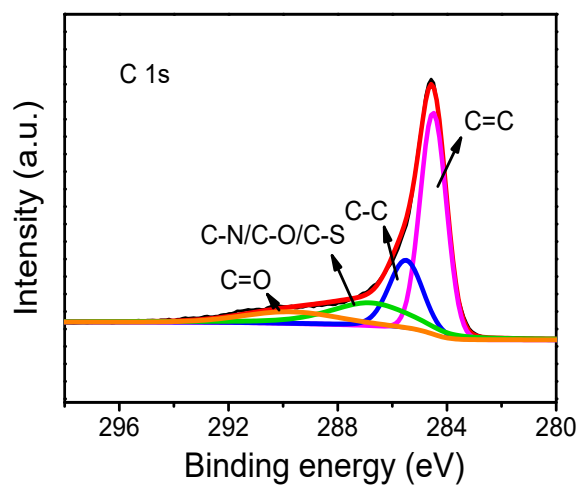
Fig. S11 The high resolution C 1s XPS spectrum of Zn-NS-C.
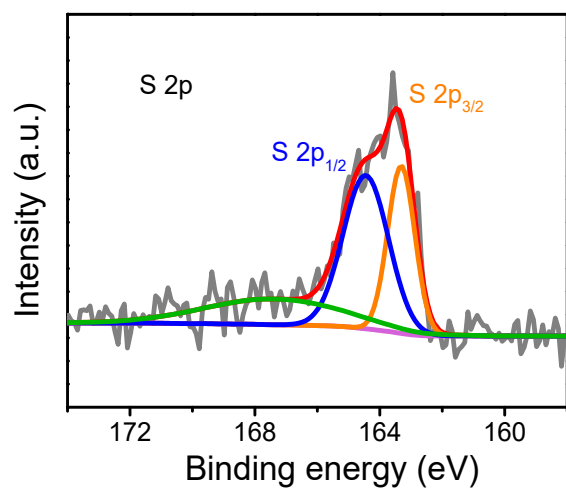
Fig. S12 The high resolution S 2p XPS spectrum of Zn-NS-C.
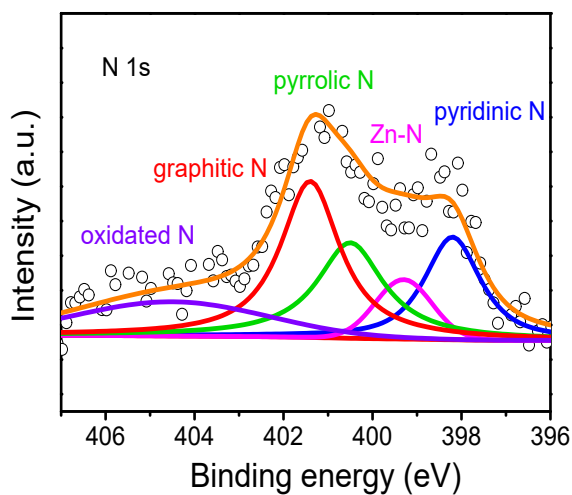
Fig. S13 The high resolution N 1s XPS spectrum of Zn-NS-C.
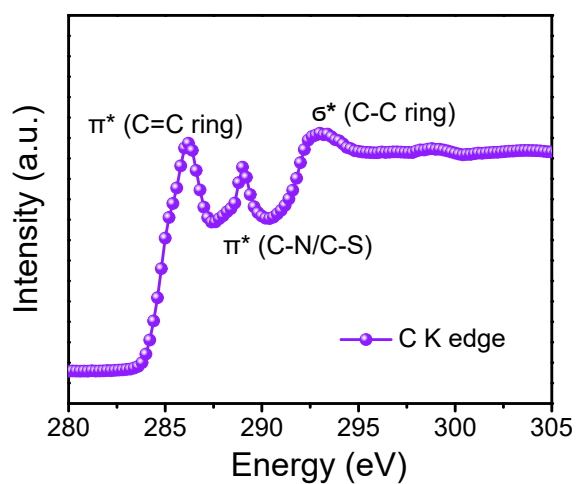
Fig. S14 The C *K*-edge spectrum of Zn-NS-C.
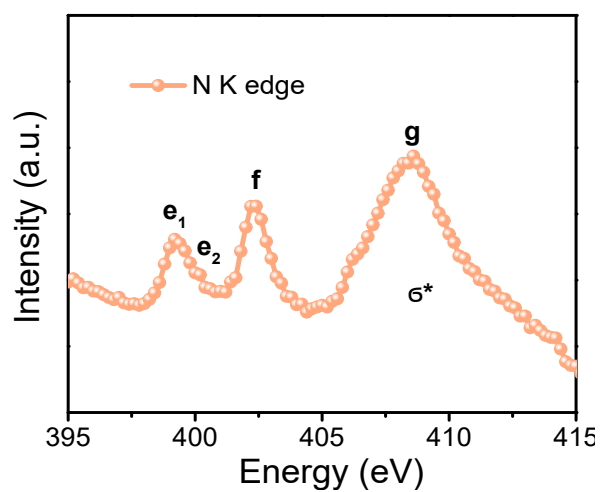
Fig. S15 The N *K*-edge spectrum of Zn-NS-C.

Zn-N$_4$-S   Zn-N$_4$-S1   Zn-N$_4$-S2
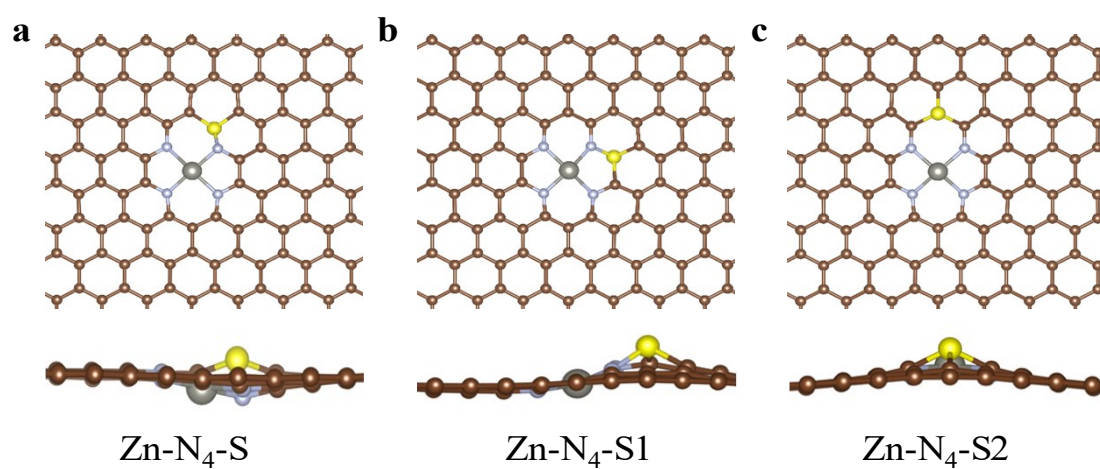
Fig. S16 Three types of coordination configuration models in Zn-NS-C.

Following the quantitative fitting results of the EXAFS spectrum, three types of configuration models that Zn-N$_4$ accompanied adjacent S atom are considered. To determine the stability of the S-doped configurations, the formation energies of S doping are calculated by:

$$\Delta E_{\mathrm{f}} \;=\; E(\mathrm{Zn \text{-} N}_4 + \mathrm{S}) + E(\mathrm{C}) - E(\mathrm{Zn} - \mathrm{N}_4) - E(\mathrm{S})$$

where E(Zn-N$_4$ + S) and E(Zn-N$_4$) are the total energy of Zn-N$_4$ with and without S doping, E(C) and E(S) are the energy of graphene and S atom. The formation energies of Zn-N$_4$-S, Zn-N$_4$-S1, and Zn-N$_4$-S2 were calculated to be -1.15, -0.87, and -0.79 eV, respectively, indicating that the Zn-N$_4$-S is the most stable one among the considered configurations. Notably, the symmetry of atomic configuration is broken after S doping, resulting in the local wrinkles and the S atom is pushed out of the graphitic layer.
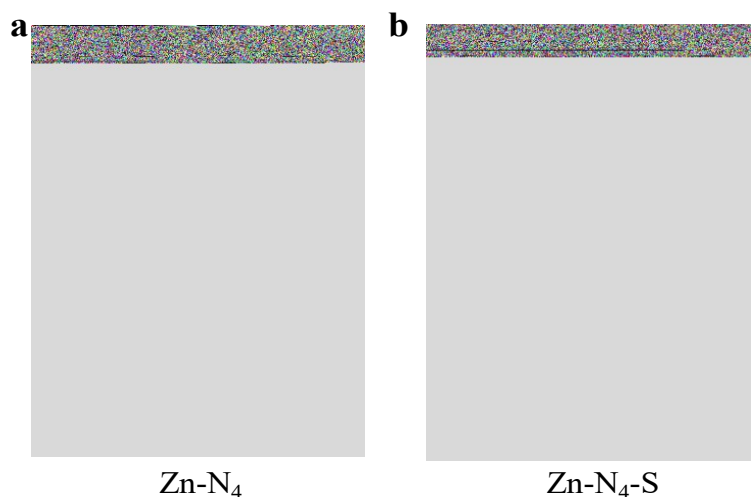
Zn-N$_4$ Zn-N$_4$-S

Fig. S17 The Bader charge distribution plots of (a) Zn-N$_4$ and (b) Zn-N$_4$-S.

The calculated changes of Bader charge distributions in the Zn-N$_4$ and Zn-N$_4$-S models (Fig. S17) showed that the lost electron numbers are decreased to 0.41 |e| after S doping, which suggests that the central Zn atom in the Zn-N$_4$-S configuration possesses a higher electron density than control Zn-N$_4$, resulting in a lower valence state of central Zn atom in Zn-N$_4$-S than Zn-N$_4$.
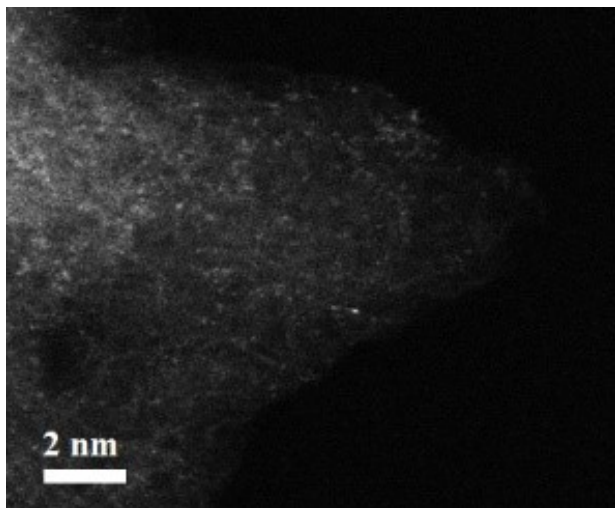
Fig. S18 The AC-HAADF STEM image of Zn-N-C.

As a contrast, the control Zn-N-C with atomically dispersed Zn-N$_4$ coordination but without S doping was also developed.
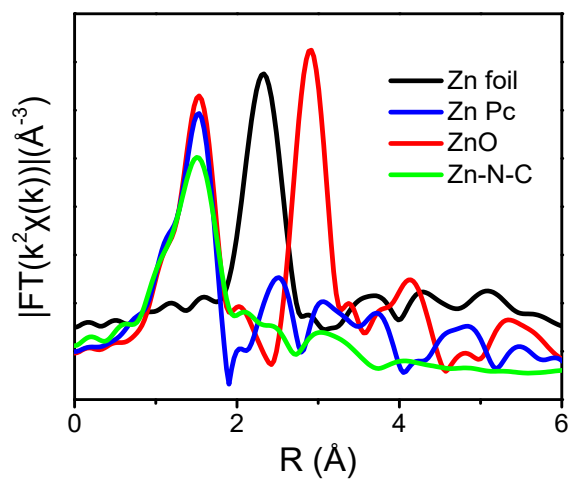

Fig. S19 The FT-EXAFS spectra of Zn foil, Zn Pc, ZnO, and Zn-N-C.
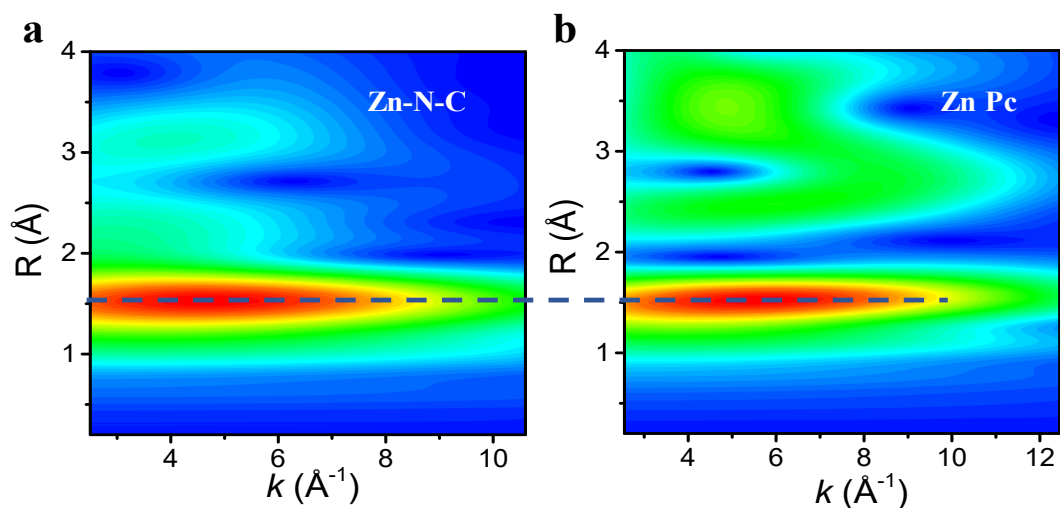
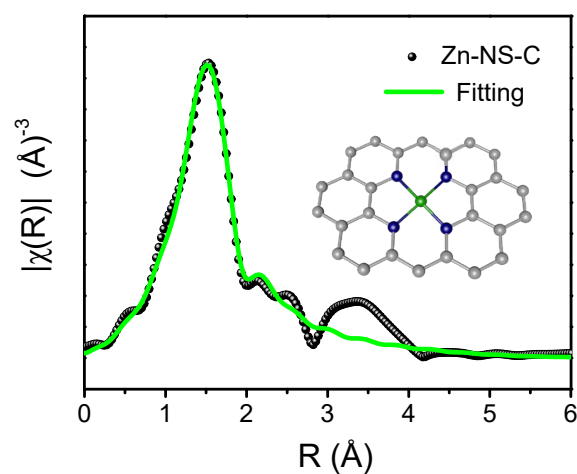**Fig. S20** The WT-EXAFS spectra of (a) Zn-N-C and (b) Zn Pc.

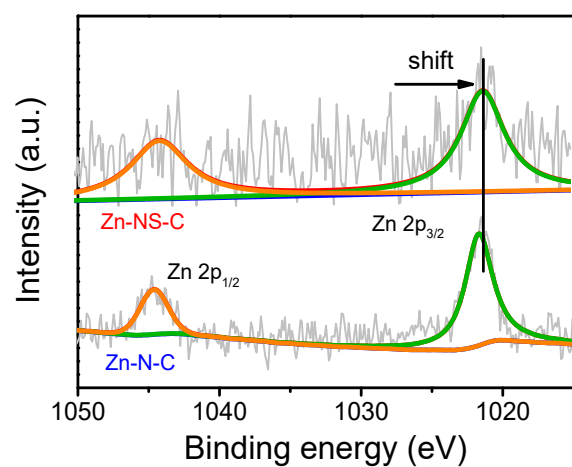**Fig. S21** The fitting results of FT-EXAFS over Zn-N-C.

Fig. S22 The high resolution Zn 2p XPS spectra of Zn-NS-C and Zn-N-C.
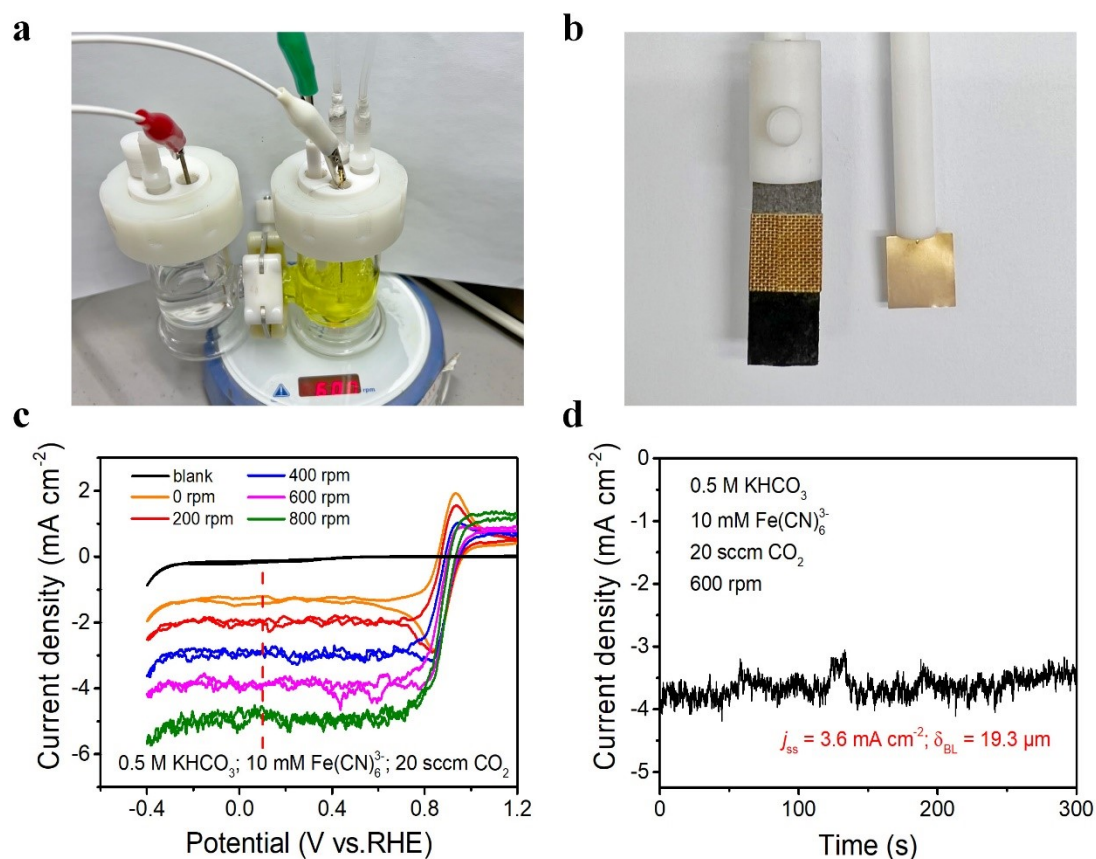
Fig. S23 (a) The digital photo of the composition of the H-cell, (b) the digital photo of the working electrode for CO_2ER test (left) and ferricyanide reduction (right), the geometrical reaction area was 1×1 cm², (c) the CV curves obtained in 0.5 M CO_2 saturated $KHCO_3$ solutions without ferricyanide (blank) and with 10 mM of ferricyanide under different stirring rates, (d) the chronoamperometry curve obtained in 0.5 M CO_2 saturated $KHCO_3$ solution with 10 mM of ferricyanide under 600 rpm stirring rate. During the test process, the CO_2 flow rate was fixed to be 20 mL min^{-1} (sccm), which is the same as the condition utilized to measure the performance of as-prepared catalysts.

In Fig. S23c, it is clearly seen that the diffusion-limited current density for ferricyanide reduction increased with increasing the stirring rate of the electrolyte, suggesting that the mass transfer effects can be eliminated to some extent by magnetic stirring the electrolyte. Therefore, the mass transfer of dissolved CO_2 could also be enhanced by stirring the electrolyte during the CO_2ER testing. Taking the potential of 0.1 V vs. RHE as an applied potential, the steady-state ferricyanide diffusion-limited current density

(j_{ss}) was measured. Under the same testing condition as that for our CO_2ER measurements (Fig. S23d), the j_{ss} was measured to be 3.6 mA cm^{-2}, thus the hydrodynamic boundary layer thickness (δ_{BL}) for ferricyanide transfer was calculated to be 19.3 μm. Along this line, the boundary layer thickness (δ_{CO2}) for dissolved CO_2 transfer was calculated to be 26.8 μm, and then the j_{limit} for CO_2-to-CO conversion ($j_{limit,CO}$) in our H-cell was finally determined to be 47 mA cm^{-2}.
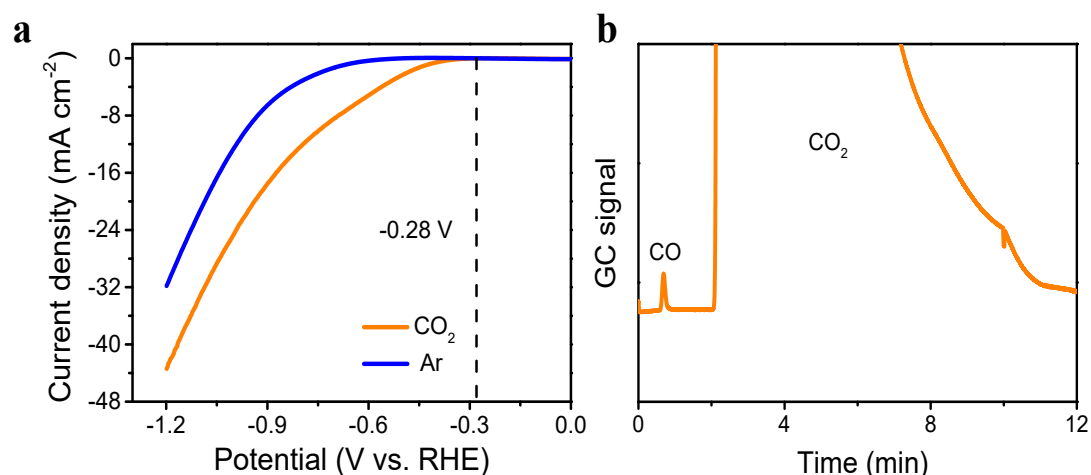

Fig. S24 (a) Linear sweep voltammetry curves of Zn-NS-C catalyzed CO_2ER in 0.5 M Ar/CO_2 saturated $KHCO_3$, (b) the CO signal detected by gas chromatography at -0.28 V.
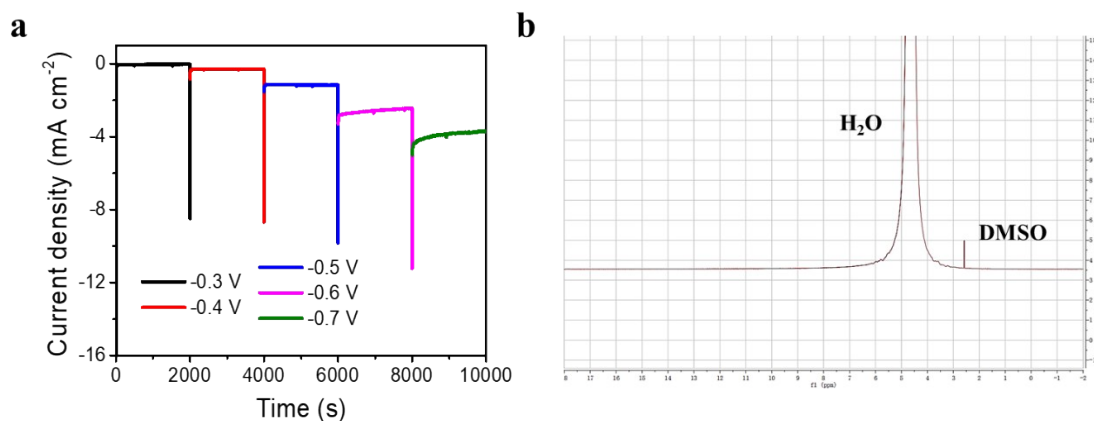
Fig. S25 (a) The multi-step i-t curves at different applied potentials of Zn-NS-C, (b) ^{1}H NMR spectrum of the electrolyte after CO_2ER test.

All the potential liquid products from CO_2ER could be detected by ^{1}H NMR spectroscopy, in which the peaks of formate, n-propanol, methanol, acetate, and ethanol can be found at the chemical shifts of 8.33, 3.44, 3.23, 1.87, and 1.06 ppm, respectively. Moreover, only peaks of the H_2O and DMSO can be found (Fig. S25b), indicating that no liquid products were produced by Zn-NS-C catalyzed CO_2ER.
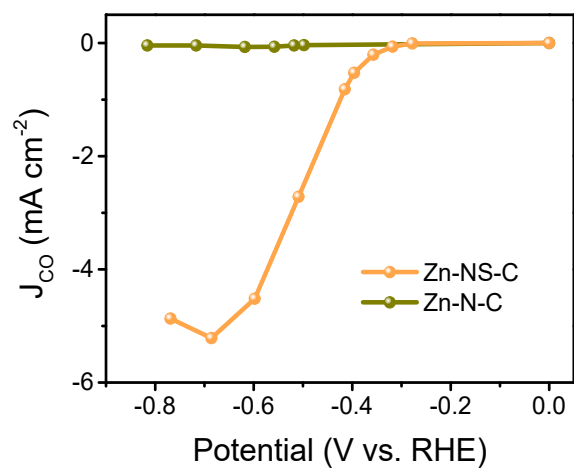
Fig. S26 The J_{CO} of Zn-NS-C and Zn-N-C catalyzed CO_2ER.

The maximum J_{CO} of Zn-NS-C was found to be 5.2 mA cm^{-2} at all the applied potentials in the H-cell (Fig. S26), which was much lower than the value of $j_{limit,CO}$ (47 mA cm^{-2}), indicating that the CO_2ER process within such applied potential range has sufficient CO_2 mass transfer.
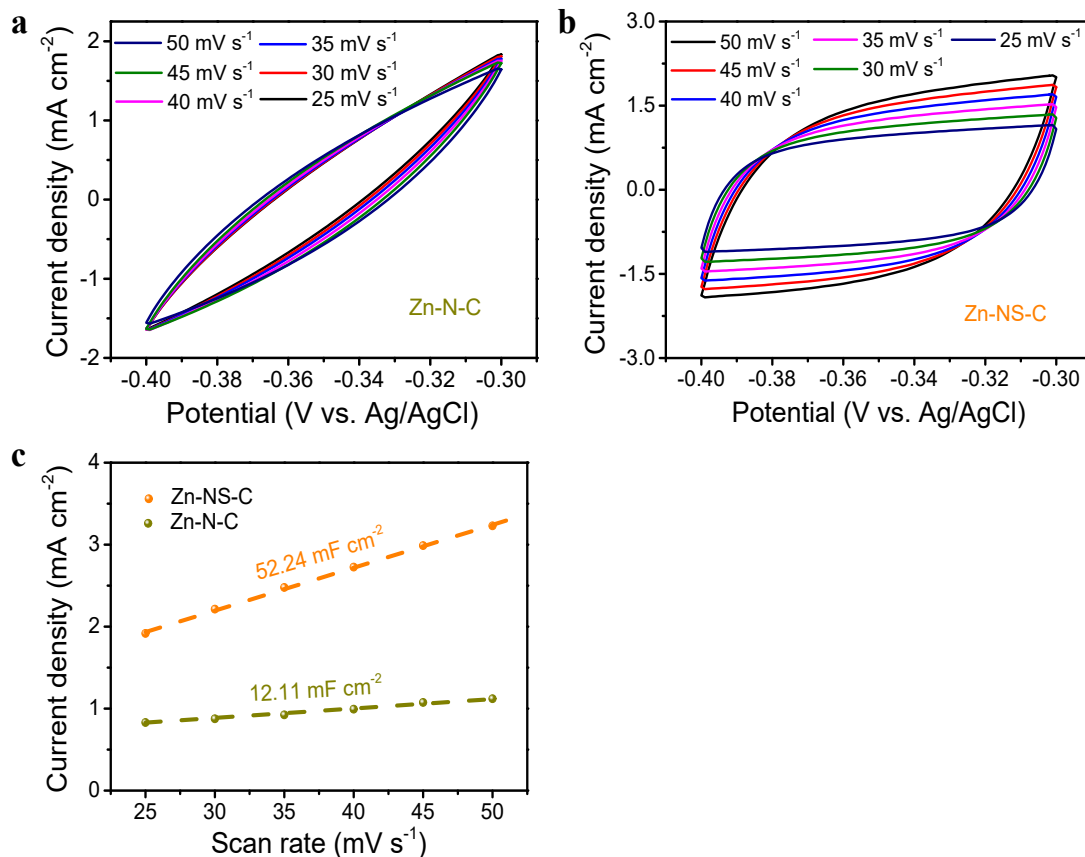
Fig. S27 The cyclic voltammetry curves of (a) Zn-N-C and (b) Zn-NS-C under applied potentials range of -0.3 to -0.4 V vs. Ag/AgCl, (c) the double layer capacitance (C_{dl}) of Zn-NS-C and Zn-N-C.

The ECSA values are calculated according to the following equation:

$$\text{ECSA} = \frac{C_{dl}}{21\,\mu\text{F cm}^{-2}} \times S$$

where 21 μF cm^{-2} is the C_{dl} of the carbon. S is the electrode area, 1.0 cm^2. Thus, the ECSA values of Zn-NS-C and Zn-N-C are calculated to be 2488 cm^2, and 577 cm^2.
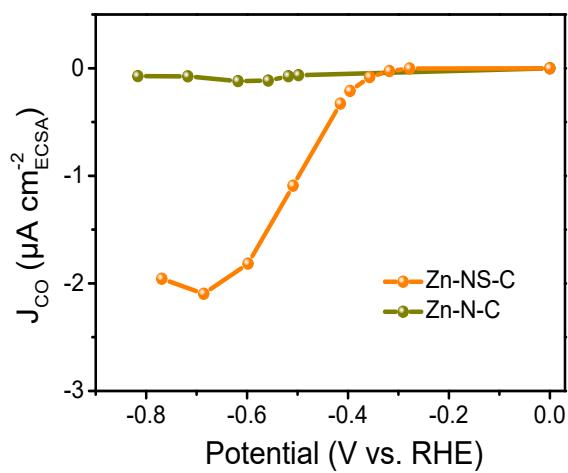
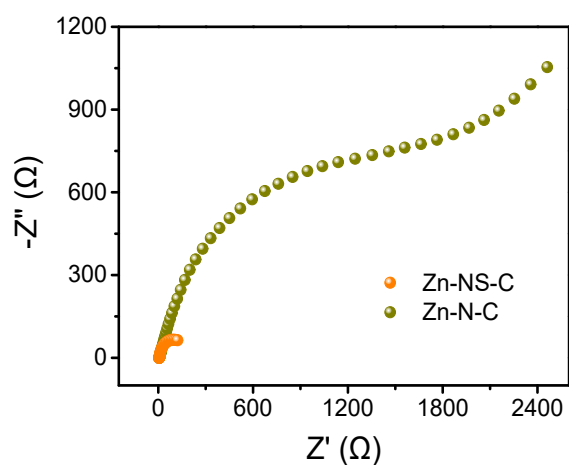**Fig. S28** The ECSA normalized J_{CO} of Zn-NS-C and Zn-N-C catalyzed CO_2ER.

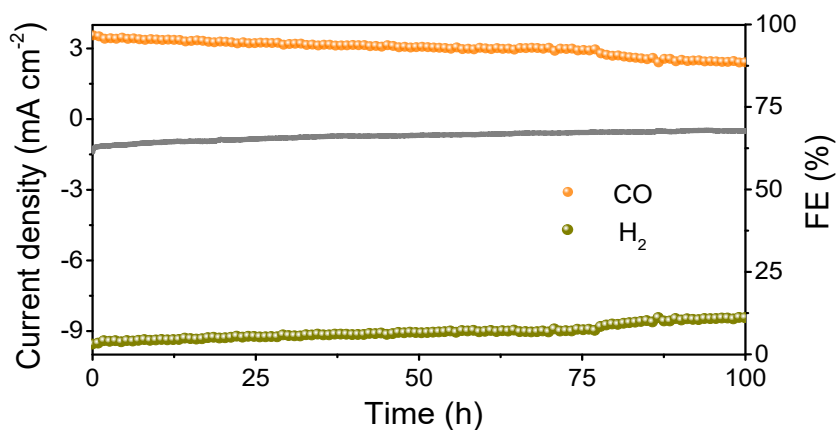**Fig. S29** The Nyquist plots of Zn-NS-C and Zn-N-C catalyzed CO_2ER.

Fig. S30 The long-term stability and CO/H$_2$ FEs of Zn-NS-C catalyzed CO$_2$ER at -0.5 V obtained in H-cell.
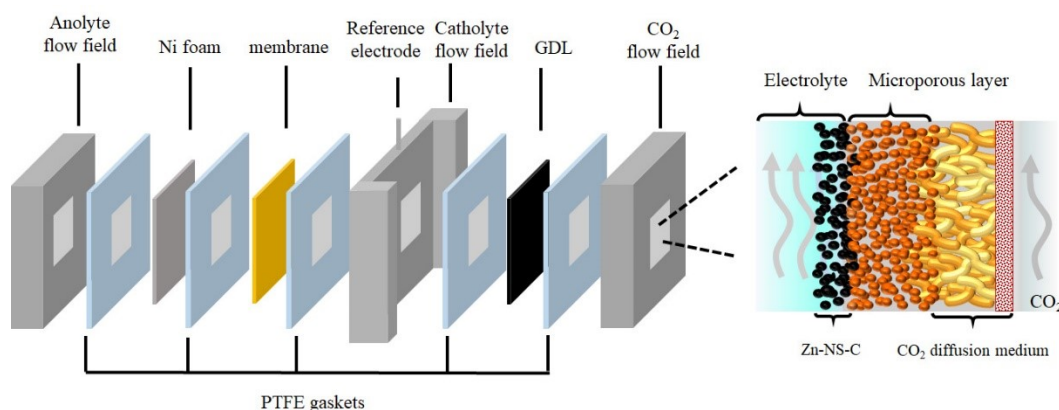

Fig. S31 The schematic diagram of the flow cell, the geometric reaction area of PTFE gaskets on the cathodic side was clipped to be 1.0×0.5 cm².
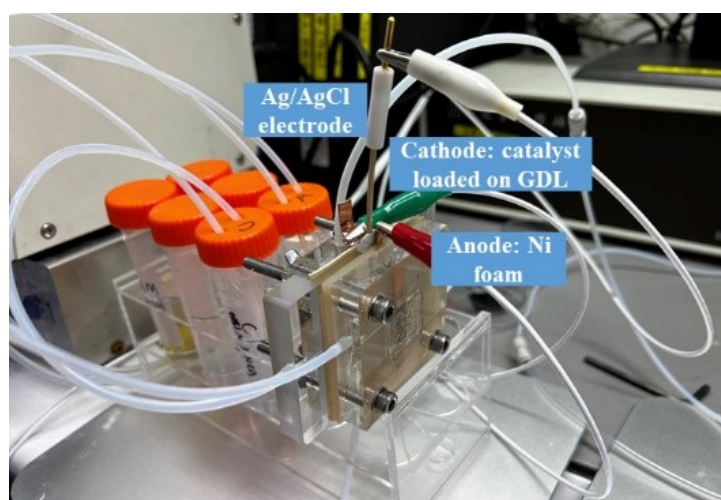

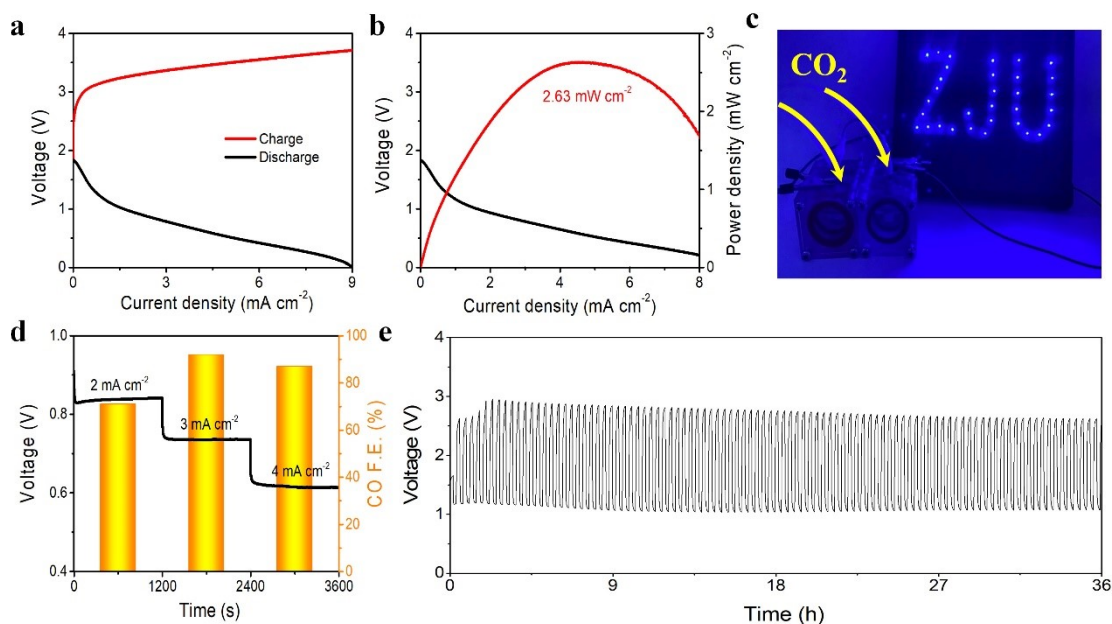**Fig. S32** The digital photo of the composition of the flow cell.

Fig. S33 The (a) charge and discharge curves, (b) discharge and power density curves of Zn-NS-C derived Zn-CO$_2$ battery, (c) the photograph of light-emitting diode powered by two Zn-CO$_2$ batteries with Zn-NS-C in series, (d) the CO FE at certain current densities, (e) the charging-discharging cycling curve at 0.5 mA cm^{-2}.

In view of superior CO$_2$ER performance of Zn-NS-C, a Zn-CO$_2$ battery equipped with Zn foil and Zn-NS-C was assembled.[15] The CO$_2$ER catalysis occurred during the discharging process in Zn-CO$_2$ battery, and the charging and discharging curves shown in Fig. S33a suggested the rechargeable feature of Zn-CO$_2$ battery. Notably, the Zn-CO$_2$ device with Zn-NS-C delivered a peak power density of 2.63 mW cm^{-2} (Fig. S33b), outperforming all the previously reported M-SAs-N-C driven Zn-CO$_2$ battery (Table S7). Two Zn-CO$_2$ batteries in series can power the light-emitting diode (Fig. S33c), indicating the effective energy output of Zn-CO$_2$ battery. Additionally, the Zn-CO$_2$ battery showed a high CO$_2$ER performance during discharging process, in which a maximum CO FE of 92% was achieved (Fig. S33d). The rechargeable also exhibited a high durability with long-term cyclic charge-discharge of 100 cycles under 0.5 mA cm^{-2} (Fig. S33e).
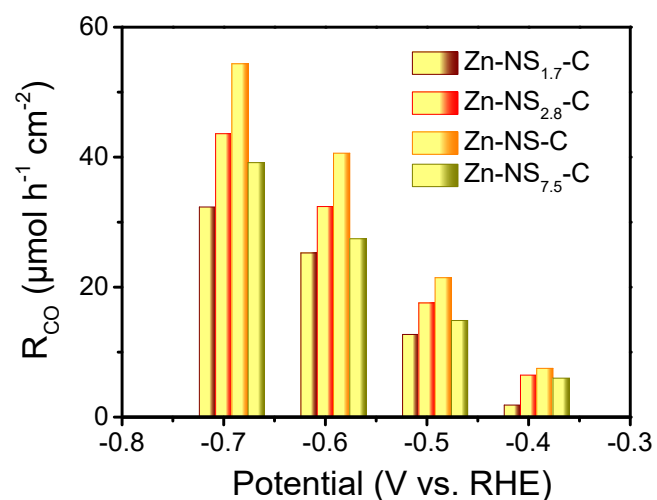
Fig. S34 The R_{CO} values of Zn-NS$_{1.7}$-C, Zn-NS$_{2.8}$-C, Zn-NS-C, and Zn-NS$_{7.5}$-C catalyzed CO$_2$ER.
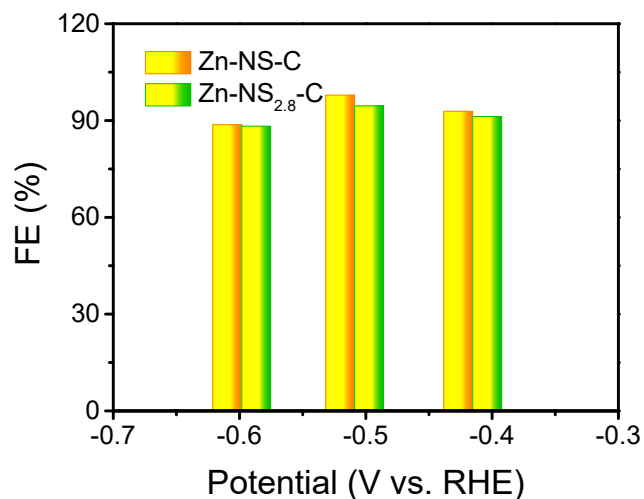

Fig. S35 The CO FEs of Zn-NS-C and Zn-NS$_{2.8}$-C catalyzed CO$_2$ER.
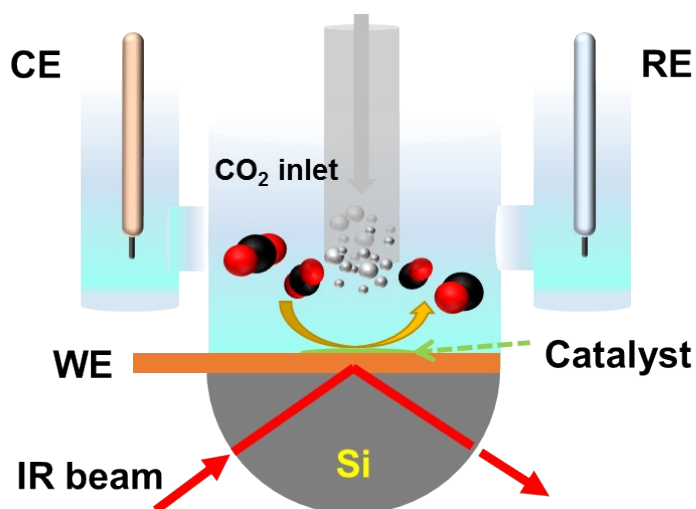
Fig. S36 The schematic diagram of *in-situ* FTIR-ATR measurements.

The spectra were detected in the CO_2-saturated 0.5 M $KHCO_3$ solution at the potential range of 0 ~ -1.2 V vs. RHE with the step interval of 0.1 V. The infrared signal intensity obtained at 0 V was used as the reference (R_0), the infrared signal intensity (Abs) at certain potential was calculated by the formula of Abs = -log(R/R_0). That is, all the signal peaks in infrared spectra detected at different potentials were based on the blank counterpart. Therefore, a negative peak represents the adsorbed species consumed, while a positive peak represents the adsorbed species accumulated.

Fig. S37 The (a) *in-situ* FTIR-ATR spectra and (b) peak area ratio of *H_2O/*COOH of Zn-NS-C catalyzed CO_2ER at different reaction time under a constant potential of -0.5 V.

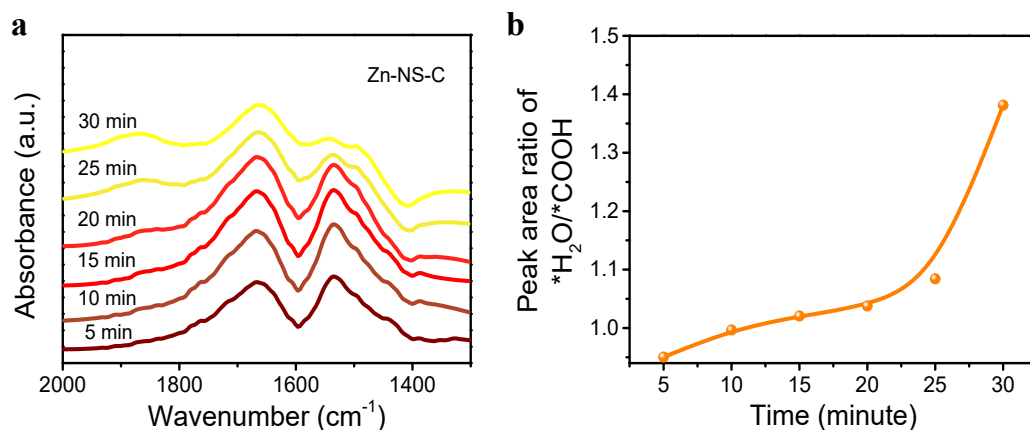The spectra were obtained at the different reaction time of 0 ~ 30 min with the step interval of 5.0 min at a certain potential of -0.5 V vs. RHE (the same potential applied as we detected the maximum CO FE). The signal intensity in infrared spectra obtained at the initial state was used as the reference, and the infrared signal intensity obtained at a certain reaction time was calculated by the formula of Abs = -log(R/R_0).

The previous Tafel slope results showed that the RDS of CO_2ER over Zn-NS-C was the protonation of *CO_2 to *COOH, while the proton donor could be H_2O and/or bicarbonate in the neutral electrolyte. In the case of H_2O acted as the proton donor in RDS (*CO_2 + e⁻ + H_2O → *COOH + OH⁻) of CO_2ER, the consumption rate of H_2O should be not less than the formation rate of *COOH because of the potential HER occurred simultaneously. When reflected in the time resolved *in-situ* FTIR-ATR spectra, the peak area ratio of *H_2O to *COOH should be lower than 1.0.
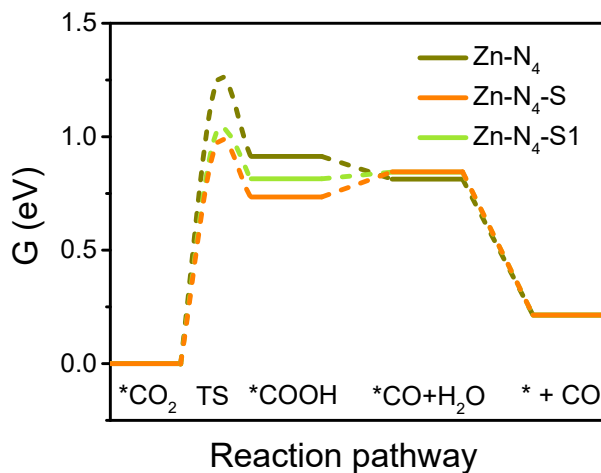
Fig. S38 The Gibbs free energy profiles of Zn-N$_4$, Zn-N$_4$-S and Zn-N$_4$-S1 catalyzed CO$_2$ER under the condition of U = 0 V and pH = 7.2.
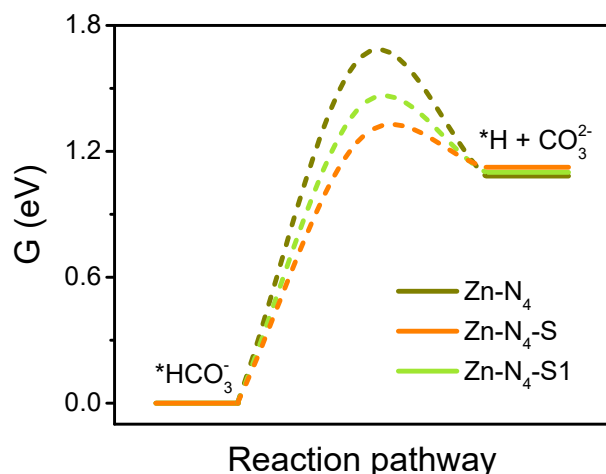
Fig. S39 The Gibbs free energies for bicarbonate dissociation on Zn-N$_4$-S model.
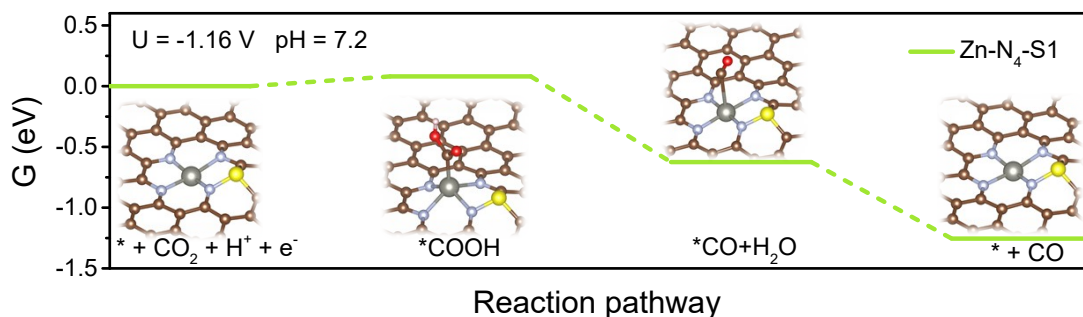
Fig. S40 The Gibbs free energy profiles and structural evolutions of Zn-N$_4$-S1 catalyzed CO$_2$ER under the condition of U = -1.16 V and pH = 7.2.
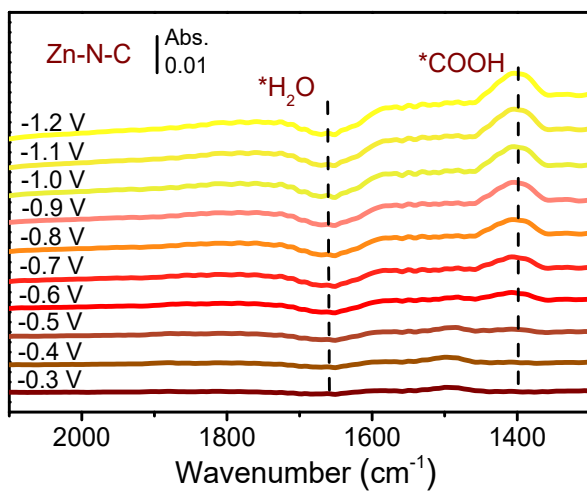
Fig. S41 The *in-situ* FTIR-ATR spectra of Zn-N-C catalyzed CO_2ER at different applied potentials.
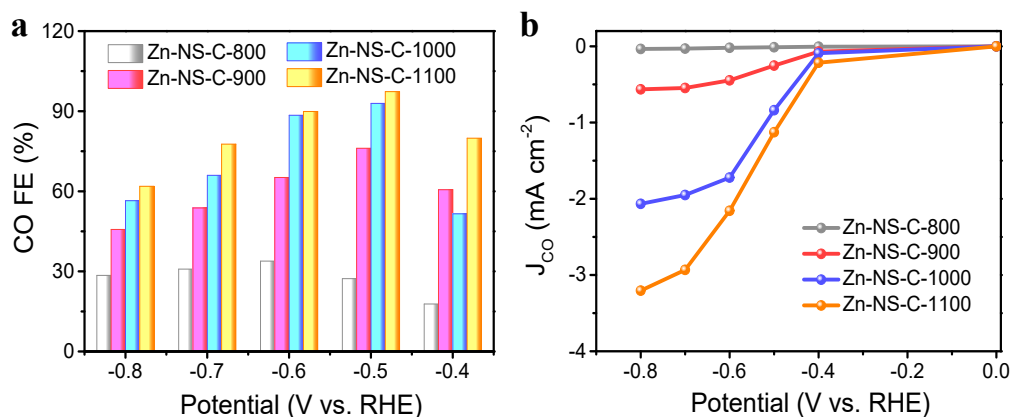
Fig. S42 The (a) CO FEs and (b) J_{CO} of Zn-NS-C-Y catalyzed CO_2ER.

The Zn-NS-C-Y samples obtained at different carbonization temperatures were synthesized. The Zn-NS-C carbonized at 1100 °C exhibited the highest CO FE and J_{CO} for CO_2ER, thus the optimal carbonization temperature was fixed to be 1100 °C.
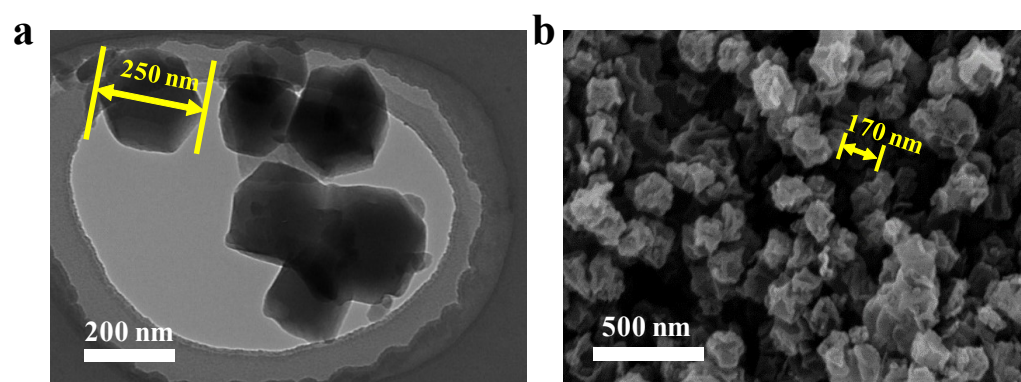
Fig. S43 FESEM images of Zn-NS-C-170 (a) before and (b) after carbonization.
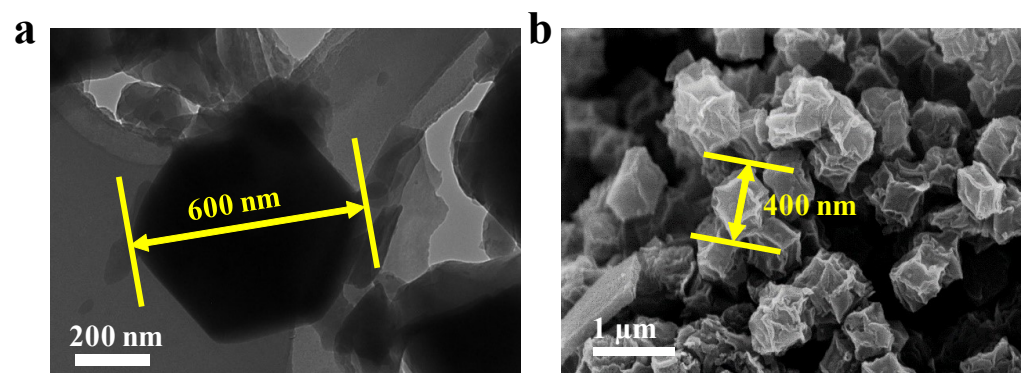
Fig. S44 FESEM images of Zn-NS-C-400 (a) before and (b) after carbonization.
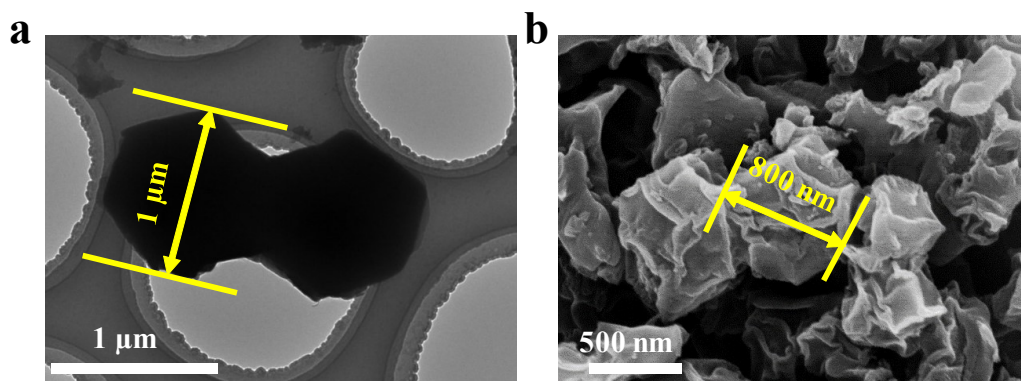
Fig. S45 FESEM images of Zn-NS-C-800 (a) before and (b) after carbonization.
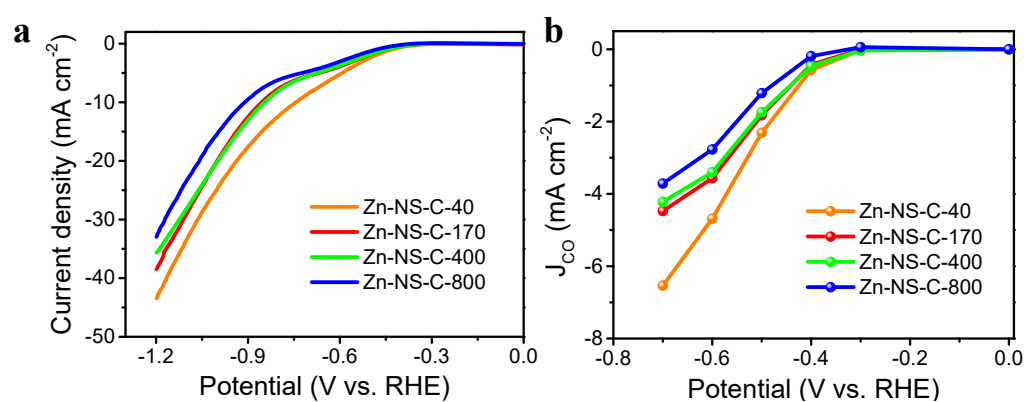
Fig. S46 (a) Linear sweep voltammetry curves and (b) J_{CO} of Zn-NS-C-Z catalyzed CO_2ER.

The Zn-NS-C-Z samples with different particle sizes were synthesized. The Zn-NS-C with particle size of 40 nm showed the highest total current density and J_{CO} for CO_2ER, thus the optimal particle size was fixed to be 40 nm.

Table S1. The Gibbs free energies for bicarbonate dissociation in different heteroatoms doped Zn-N$_4$ models.

Heteroatom	Gibbs free energy for *HCO$_3^-$ → *H + CO$_3^{2-}$ (eV)	TS (eV)
B	1.63	1.68
P	1.59	1.70
S	1.12	1.32

Table S2. The content of Zn atoms in Zn-NS-C, Zn-NS$_{2.8}$-C and Zn-N-C quantified by ICP-OES tests.

Sample	Zn content (wt.%)
Zn-NS-C	0.2
Zn-NS$_{2.8}$-C	0.17
Zn-N-C	1.04

Table S3. The quantitative fitting results of FT-EXAFS spectra of Zn-NS-C, Zn-N-C, and Zn Pc.

Sample	Shell	Bond length (Å)	C.N.	ΔE_0 (eV)	σ^2 (Å^2)	S_0^2	R-factor
Zn Pc	Zn-N	1.99(1)	4	2.6(1)	0.005(1)	1.12(1)	0.008
	Zn-C	2.99(1)	8		0.008(2)		
Zn-NS-C	Zn-N	2.01(1)	5.1(6)	-1.2(1)	0.012(2)	1.12	0.011
	Zn-S	3.03(3)	0.41(1)		0.004		
Zn-N-C	Zn-N	2.01(1)	5.3(5)	3.8(1)	0.011(1)	1.12	0.007

$^\delta$ C.N. is the coordination number.

Table S4. The theoretical bond lengths of Zn-N, and the atomic distances between Zn and S atoms in Zn-N$_4$-S, Zn-N$_4$-S1, and Zn-N$_4$-S2.

Configuration model	Zn-N bond length (Å)	Zn/S interatomic distance (Å)
Zn-N$_4$-S		3.08
Zn-N$_4$-S1	2.0	2.93
Zn-N$_4$-S2		3.49

Table S5. The comparison of the maximum TOF values over Zn-NS-C and other reported Zn-SAs-N-C catalysts.

Sample	TOF (h^{-1})	Reactor	Membrane	Electrolyte	Ionomer for binding catalysts on carbon paper	Catalyst loading amount (mg cm^{-2})	Reaction area (cm^2)	Refs.
Zn-NS-C	**11419**	**H-cell**	**Nafion 117**	**0.5 M KHCO$_3$**	**Nafion solution**	**0.20**	**1.0**	this work
Zn$^{\delta+}$-NC	875	H-cell	N.A.	0.5 M KHCO$_3$	Nafion solution	0.25	**1.0**	[16]
Zn SAs/N-C	8190	H-cell	N.A.	0.5 M KHCO$_3$	Nafion solution	1.50	**1.0**	[17]
ZnN$_x$/C	9969	H-cell	Nafion 117	0.5 M KHCO$_3$	Nafion solution	1.00	**1.0**	[18]
SA-Zn-NHPC	10113	H-cell	Nafion 115	0.5 M KHCO$_3$	Nafion solution	1.00	**1.0**	[19]

Table S6. The cathodic potentials, J_{total}, CO FEs, and J_{CO} of Zn-NS-C obtained in flow cell, the anolyte and catholyte were circulated 1.0 M $KHCO_3$ solution with a flow rate of 10 mL min^{-1}.

Potentials (V vs. RHE)	J_{total} (mA cm^{-2})	CO FEs (%)	J_{CO} (mA cm^{-2})
-0.38	40	98.5	39.4
-0.41	120	99.8	119.8
-0.55	200	99.6	199.2
-0.59	240	94.9	227.8
-0.61	280	93.4	261.5
-0.74	320	86.9	278.1

The values of J_{CO} were calculated by the formula of $J_{CO} = J_{total} \times CO\ FE/100$

Table S7. The comparison of peak power density in Zn-CO_2 battery with other reported M-SAs-N-C materials.

Sample	Peak power density (mW cm^{-2})	Refs.
Zn-NS-C	**2.63**	**this work**
Fe$_1$NC/S$_1$-1000	0.53	[20]
Co SAs@NCMF	0.61	[21]
DNG-SAFe	0.90	[22]
Cu-N$_2$/GN	0.62	[23]
Ni-N$_3$-NCNFs	1.05	[15]
NOMC	0.71	[24]
CoPc@DNHCS-8	1.02	[25]
Zn/NC NS	1.8	[26]

Table S8. The detailed synthetic conditions for preparing Zn-NS-C and Zn-NS$_x$-C.

Sample	ZIF-8 : Linker mass ratio	Time for linker exchange (h)	Carbonization temperature (ºC)	S Content (wt.%)
Zn-NS$_{1.7}$-C	1:2	0.5		1.7
Zn-NS$_{2.8}$-C	1:2	24		2.8
Zn-NS-C	1:2	48	1100	4.5
Zn-NS$_{7.5}$-C	1:3	48		7.5

References

1.   L. Clark, J. Resasco, A. Landers, J. Lin, L.-T. Chung, A. Walton, C. Hahn, T. F. Jaramillo and A. T. Bell, *ACS Catal.,* 2018, **8**, 6560-6570.

2.   K. Williams, N. Corbin, J. Zeng, N. Lazouski, D.-T. Yang and K. Manthiram, *Sustain. Energy Fuels,* 2019, **3**, 1225-1232.

3.   G. Kresse and J. Furthmüller, *Phys. Rev. B.*, 1996, **54**, 11169-11186.

4.   G. Kresse and D. Joubert, *Phys. Rev. B.*, 1999, **59**, 1758-1775.

5.   J. P. Perdew, K. Burke and M. Ernzerhof, *Phys. Rev. Lett.*, 1996, **77**, 3865-3868.

6.   S. Grimme, J. Antony, S. Ehrlich and H. Krieg, *J. Chem. Phys.*, 2010, **132**, 154104.

7.   H. J. Monkhorst and J. D. Pack, *Phys. Rev. B.*, 1976, **13**, 5188-5192.

8.   V. Wang, N. Xu, J.-C. Liu, G. Tang and W.-T. Geng, *Comput. Phys. Commun.*, 2021, **267**, 108033.

9.   K. Mathew, R. Sundararaman, K. Letchworth-Weaver, T. A. Arias and R. G. Hennig, *J. Chem. Phys.,* 2014, **140**, 084106.

10. G. Henkelman, B. P. Uberuaga and H. Jónsson, *J. Chem. Phys.,* 2000, **113**, 9901-9904.

11. Q. Wang, T. Ina, W.-T. Chen, L. Shang, F. Sun, S. Wei, D. Sun-Waterhouse, S. G. Telfer, T. Zhang and G. I. N. Waterhouse, *Sci. Bull.,* 2020, **65**, 1743-1751.

12. M. Erkartal, U. Erkilic, B. Tam, H. Usta, O. Yazaydin, J. T. Hupp, O. K. Farha and U. Sen, *Chem. Commun.,* 2017, **53**, 2028-2031.

13. X. Li, C.-S. Cao, S.-F. Hung, Y.-R. Lu, W. Cai, A. I. Rykov, S. Miao, S. Xi, H. Yang, Z. Hu, J. Wang, J. Zhao, E. E. Alp, W. Xu, T.-S. Chan, H. Chen, Q. Xiong, H. Xiao, Y. Huang, J. Li, T. Zhang and B. Liu, *Chem*, 2020, **6**, 3440-3454.

14. L. Zhang, J. Wang, H. Wang, W. Zhang, W. Zhu, T. Du, Y. Ni, X. Xie, J. Sun and J. Wang, *Nano Res.,* 2020, **14**, 1523-1532.

15. W. Zheng, Y. Wang, L. Shuai, X. Wang, F. He, C. Lei, Z. Li, B. Yang, L. Lei, C. Yuan, M. Qiu, Y. Hou and X. Feng, *Adv. Funct. Mater.*, 2021, **31**, 2008146.

16. S. Li, S. Zhao, X. Lu, M. Ceccato, X. M. Hu, A. Roldan, J. Catalano, M. Liu, T. Skrydstrup and K. Daasbjerg, *Angew. Chem. Int. Ed.*, 2021, **60**, 22826-22832.

17. M. Fang, X. Wang, X. Li, Y. Zhu, G. Xiao, J. Feng, X. Jiang, K. Lv and W.-F.

Lin, *ChemCatChem*, 2021, **13**, 603-609.

18. F. Yang, P. Song, X. Liu, B. Mei, W. Xing, Z. Jiang, L. Gu and W. Xu, *Angew. Chem. Int. Ed.*, 2018, **57**, 12303-12307.

19. N. Wang, Z. Liu, J. Ma, J. Liu, P. Zhou, Y. Chao, C. Ma, X. Bo, J. Liu, Y. Hei, Y. Bi, M. Sun, M. Cao, H. Zhang, F. Chang, H.-L. Wang, P. Xu, Z. Hu, J. Bai, H. Sun, G. Hu and M. Zhou, *ACS Sustain. Chem. Eng.*, 2020, **8**, 13813-13822.

20. T. T. Wang, X. H. Sang, W. Z. Zheng, B. Yang, S. Y. Yao, C. J. Lei, Z. J. Li, Q. G. He, J. G. Lu, L. C. Lei, L. M. Dai and Y. Hou, *Adv. Mater.*, 2020, **32**, 9.

21. Y. Zhao, Z. Pei, X. F. Lu, D. Luan, X. Wang and X. W. Lou, *Chem Catal.*, 2022, **2**, 1480-1493.

22. W. Ni, Z. Liu, Y. Zhang, C. Ma, H. Deng, S. Zhang and S. Wang, *Adv. Mater.*, 2021, **33**, e2003238.

23. Y. Hou, M. Qiu, M. G. Kim, P. Liu, G. Nam, T. Zhang, X. Zhuang, B. Yang, J. Cho, M. Chen, C. Yuan, L. Lei and X. Feng, *Nat. Commun.*, 2019, **10**, 1392.

24. S. Gao, Y. Liu, Z. Xie, Y. Qiu, L. Zhuo, Y. Qin, J. Ren, S. Zhang, G. Hu, J. Luo and X. Liu, *Small Methods*, 2021, **5**, e2001039.

25. S. Gong, W. Wang, C. Zhang, M. Zhu, R. Lu, J. Ye, H. Yang, C. Wu, J. Liu, D. Rao, S. Shao and X. Lv, *Adv. Funct. Mater.*, 2022, **32**, 2110649.

26. J. Chen, Z. Li, X. Wang, X. Sang, S. Zheng, S. Liu, B. Yang, Q. Zhang, L. Lei, L. Dai and Y. Hou, *Angew. Chem. Int. Ed.*, 2022, **61**, e202111683.